J. Phys. Chem. A **2003,** *107,* 10615−10624 **10615**

Sticking of Hyperthermal CO to the (0001) Face of Crystalline Ice[†]

A. Al-Halabi,[‡] A. W. Kleyn,[‡] E. F. van Dishoeck,[§] M. C. van Hemert,[‡] and G. J. Kroes*[,‡]

Leiden Institute of Chemistry, Gorlaeus Laboratories, P.O. Box 9502, 2300 RA Leiden, The Netherlands, and Leiden Observatory, P.O. Box 9513, 2300 RA Leiden, The Netherlands

Received: March 26, 2003; In Final Form: September 15, 2003

We present the results of classical trajectory calculations on the sticking of hyperthermal CO to the basal plane (0001) face of ice I_h, for normal and off-normal incidence at surface temperature (T_s) = 150 K. The sticking probability decreases with the incidence energy (E_i) and with the incidence angle (θ_i) for $\theta_i > 20°$. At normal incidence, the sticking probability can be fitted to a simple decay function: $P_s = 0.9\ e^{-0.012E_i(\mathrm{kJ/mol})}$. The energy transfer from the impinging molecule to the surface is found to be efficient and fast: most of E_i is transferred to the surface within 0.5−1.0 ps. For off-normal incidence, the energy transfer becomes less efficient for $\theta_i > 20°$. In the case of backscattering at off-normal incidence, the hotter molecules scatter at larger angles. At high E_i, no surface penetration occurs, but the impinging molecule may damage the surface significantly when it hits the surface in the center of a hexagonal ring. The energy minimization calculations suggest that CO is adsorbed either on top of an OH dangling group, or on top of the center of a water hexagonal ring, interacting mostly with an electron lone-pair oxygen atom in the first monolayer or with a four-coordinated oxygen in the second monolayer. The molecular dynamics calculations predict that the average binding energy of the adsorbed CO is 4.33 kJ/mol, with a maximum value of 10.4 kJ/mol. The results of our calculations are compared with the experimental and the previous theoretical data on the CO−ice and N_2−ice systems.

1. Introduction

Chemical reactions on ice surfaces play an important role in a variety of environments. Reactions relevant to atmospheric chemistry include, for instance, reactions between so-called “chlorine passivated compounds”, namely, HCl and $ClONO_2$. These reactions, which occur on ice surfaces provided by polar stratospheric clouds in winter time,[1−3] activate the chlorine which starts destroying ozone via catalytic gas-phase reactions by the return of the sunlight in the spring,[1−4] causing the infamous ozone hole.

With regard to the interstellar medium (ISM), the chemistry on ice surfaces has also received a lot of discussion. In the ISM, the dust grain particles may have icy mantles consisting mainly of H_2O but also of other molecules such as CO, CO_2, NH_3, and CH_4, which accumulate on the cores of solid particles consisting of silicates and carbonaceous compounds.[5] Infrared (IR) spectra revealed that water and carbon monoxide are the most abundant molecules in the icy mantled particles in the ISM.[6−9] The sticking of CO to water ice is therefore important to our understanding of how the icy mantles coating the grain particles are formed. As will be discussed below, it is also relevant to the chemistry on the icy mantles.

The icy mantles are believed to have an amorphous structure.[10] However, a phase transition of the deposited water ice from the amorphous to the crystalline phase was found to occur above 110 K.[11] In the ISM, this phase transition can happen through the impact of cosmic rays. Recent experiments revealed a new, nonthermal and indirect mechanism of UV light induced crystallization of monolayer and multilayer films of amorphous ice, deposited on graphite at low surface temperatures (T_s < 100 K).[12] The experiments show that the UV light photoexcites the electrons in the substrate, which in turn tunnel to defect states in the amorphous ice, to induce exothermic crystallization. The results of these experiments may have an impact on the ideas concerning the structure of the ice surface in the ISM, in particular, for regimes where UV photons penetrate, and studies on both amorphous and crystalline ice surfaces are needed. Also, the Infrared Space Observatory (ISO) detected an emission feature at 60 μm from the disk surrounding the young star HD 100546, which clearly indicates the presence of crystalline ice[13] in the ISM.

Sticking of CO to ice is also relevant to the formation of CO_2. The presence of CO_2 ice in the ISM was first suggested by d’Hendecourt and Jourdain de Muzion (1989)[14] and observed later to be ubiquitous by the ISO.[15−17] Most CO_2 is present in the solid form, with a very low abundance in the gas phase,[18] suggesting that CO_2 molecules are formed in chemical reactions on or in the ice surfaces and frozen there because of the low temperature. Note that CO_2 was found in ices dominated by polar molecules (H_2O) as well as in ices dominated by nonpolar molecules (CO and CO_2 itself).[16]

The formation of the solid phase of CO_2 could occur via two different channels. The first channel is the formation of CO_2 by the UV photolysis of mixed ice containing CO and H_2O.[19−21] This mechanism is probably dominant in the case of the formation of solid CO_2 present in the polar ice. The results of measured rates of conversion of CO to CO_2 suggest efficient formation of CO_2 from $D_2O(H_2O)$:CO mixed ice induced by UV irradiation.[21−23] In this mechanism, a water molecule is photolyzed, and the produced OH fragment reacts with an adsorbed CO molecule to produce CO_2. There are other possible

---

[†] Part of the special issue “Charles S. Parmenter Festschrift”.

* To whom correspondence should be addressed.

[‡] Leiden Institute of Chemistry.

[§] Leiden Observatory.

10.1021/jp030374p CCC: $25.00

reaction channels for CO_2 formation in $CO:H_2O$ mixed ice by UV photolysis, involving the reactions between the CO molecules and the photodissociation of water to produce fragments other than OH (see ref 21 for more details). However, the mechanism involving OH above was considered to be the most likely mechanism,[21] because the cross section of CO_2 formation by $CO + CO$ reactions is very small[24] and because the main set of products of water photodissociation is $OH + H$, rather than $O + H_2$.[25,26] In the mechanism considered to be dominant, the formation rate of CO_2 depends on the sticking probability of CO to ice, the binding energy of CO adsorbed on or in the ice, and the lifetime of the adsorbed molecule.

The second channel involves the reaction of CO with atomic oxygen as suggested by Whittet et al.,[15,27] which is expected to be the dominant reaction in the case of nonpolar ice. Subsequent experiments performed by Roser et al. suggest that indeed CO_2 is formed when O atoms are deposited onto CO ice.[28]

Carbon monoxide has been used as a probe of several solid surfaces such as metals and metal oxides[29,30] (See also ref 31 for a partial list of such studies). Carbon monoxide can also be used among other molecules (see the theoretical survey of the adsorption of trace gases on liquid and solid water surfaces[32]) to probe the adsorbing sites of the ice surfaces and their geometrical areas (amorphous and crystalline), without perturbing the surface significantly,[31−35] because CO has a small dipole moment and a low affinity for water. However, the interaction of CO with ice is surrounded by controversy.

The infrared profile of CO trapped in (or on) an ice lattice at 10 K shows a main feature at about 2138 cm^{-1} (major band) and a secondary feature with lower intensity at 2152 cm^{-1} (minor band).[23] The main feature was initially attributed to substitutional CO, i.e., CO replacing a water molecule, and the secondary feature was attributed to interstitial CO, i.e., CO between the water molecules.[23] However, more recent experiments[36] assigned the two bands to different CO−ice configurations. The major band at 2138 cm^{-1} was assigned to CO absorbed in the ice micropores, and the minor band at 2152 cm^{-1} was assigned to CO molecules interacting with the dangling OH (referred to as dH sites).[36] The assignment of the minor band to CO interacting with the dangling OH groups was later confirmed by infrared spectroscopic experiments performed by Palumbo.[37]

Adsorption isotherms FT-IR experiments combined with ab initio calculations[31] likewise assigned the minor band to CO interacting with a dangling OH, with CO being oriented perpendicularly to the surface with its C atom toward the OH. However, in this work, the major band was also assigned to perpendicular CO interacting with a dangling OH, but with the O atom of CO toward the OH. In calculations not taking into account the basis set superposition error (BSSE), the two orientations of CO−ice and OC−ice were found to be energetically equivalent, with an adsorption energy of about 10 kJ/mol. When the energies were corrected for the BSSE,[38] the OC−ice configuration was found to be more stable. However, the values of the corrected adsorption energies were considered not to be accurate yet.[31]

Recent simultaneous measurements of isotherms by volumetric and infrared spectroscopy[33] showed that the minor band is indeed due to CO interacting with dangling OH groups. The major band was however suggested to be due to CO molecules interacting with the oxygen atoms of the pore surface rather than another orientation of CO interacting with dangling OH, as proposed earlier by Allouche et al.[31] In the new experiments, the adsorption energy of CO adsorbed on ice was found to be equal to 10.4 kJ/mol,[33] in agreement with the calculations of Allouche et al.[31]

Even more recent measurements again confirmed the assignment of the minor band to CO adsorbed on dangling OH groups, but the major band was now attributed to CO−CO interactions occurring in the case of multilayer formation as well as to interactions with the ice surface[34,35,39] at low coverage. The adsorption energy of CO was measured to be about 10−11 kJ/mol,[34,35,39] in good agreement with earlier results.[31,33] In those experiments, two additional adsorbing sites were identified, namely, the dangling electron pair oxygen atoms in the first monolayer (referred to as dO sites[40]), and the oxygen atoms of four-coordinated water molecules in the second monolayer (referred to as 4s sites[40]).[35,39] Temperature programmed desorption (TPD) and reflection−absorption infrared spectroscopy (RAIRS) experiments performed to study the adsorption and desorption of CO on and from amorphous ice (high and low-density ice) also assigned the minor band to dangling OH bonds and the major band to CO multilayer formation.[41]

Quantum calculations based on density functional theory (DFT), combined with the earlier set of the FT-IR measurements mentioned above,[39] concluded that the surface contribution to the major band is due to the CO interaction with the dO and the s4 adsorbing sites. The calculations also found the third adsorption site suggested by the experiment, attributing the minor band to CO adsorbed perpendicularly on dangling OH sites, preferably via its C atom (the binding energy being 11.4 kJ/mol for this configuration, compared to 6.3 kJ/mol for the other orientation of CO[39]).

According to molecular dynamics simulations on the adsorption of CF_4 to ice, CF_4 is adsorbed on top of the hexagonal rings, blocking the water shafts and leaving the adsorbing sites on the OH dangling groups empty.[42] The experiments showed that when CO is adsorbed on ice covered with CF_4, the minor band (due to CO adsorbed on dangling OH groups) appears first and the signal due to the minor band actually becomes larger than that due to the major band, in contrast to the case of CO adsorbed on a clean ice surface.[35,36] Also, the signals which correspond to the blocked dO and 4s adsorbing sites become smaller compared to the case of clean ice, similar to the signal associated with the major band.[35] At higher coverage of CO, the major band becomes again dominant, similar to the case of CO adsorption on clean ice.

The ab initio calculations performed by Allouche et al. also addressed the CO diffusion inside the ice through the surface hexagonal shafts.[31] In those calculations, the ice lattice was represented by two superimposed bilayers of perfectly ordered water molecules, see Figure 6 of ref 31. The calculations showed that the least unfavorable configuration of CO in ice corresponds to CO nearly perpendicular to the ice slab, in the middle of a hexagonal ring at an equidistance from both bilayers. However, this configuration is 78 kJ/mol higher than the sum of the (uncorrected) energies of the noninteracting subsystems. The calculations showed that CO cannot diffuse inside the surface through the hexagonal shafts.[31]

In this paper, we present the results of classical trajectory calculations on sticking of CO to the basal plane surface (0001) of crystalline ice at hyperthermal energies. To allow testing by molecular beam experiments, the calculations were performed for $T_s = 150$ K, a surface temperature at which molecular beam experiments on the sticking of atoms and molecules to ice surfaces have been performed previously.[43−45] We have compared our results to the results of molecular beam experiments[43] on the similar molecule, N_2, scattering from ice at hyperthermal

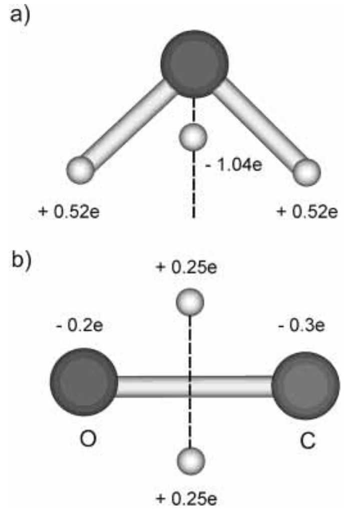

Figure 1. Point charge model for H_2O used in the TIP4P pair potential (a) and the point charge model used for CO (b). In the TIP4P model, the O−H bond is 0.96 Å and the H−O−H angle is 104.5°. The negative charge is placed at 0.15 Å from the O atom along the bisector of the H−O−H angle. In the CO model, the small spheres represent the off-axis positive point charges, which are above and below the molecular center of mass by 0.75 Å. The CO bond is 1.128 Å. The large gray sphere represents the C atom, and the black one represents the O atom. The charge $e = 1.6 \times 10^{-19}$ coulomb.

energies. Our results are also compared with the results of classical trajectory calculations on sticking of HCl to ice at hyperthermal energies.[46] The sticking probability of CO to ice is studied at different incidence energies and different angles of incidence. The sticking of thermal CO to amorphous and crystalline ice at lower, astrochemically relevant temperatures has also been studied and the results will be published elsewhere.[47,48] This paper is organized as follows. In section 2, we present the method used in this study. The results are presented and discussed in section 3, and the conclusions are offered in Section 4.

2. Method

To simulate the sticking of CO to crystalline ice, classical trajectory (CT) calculations were performed.[49] We have essentially followed the same approach as used before to study the sticking of HCl to ice.[46,50]

2.1. The Ice Surface. The ice surface was modeled using the molecular dynamics (MD) method.[51] The surface was modeled by 4 bilayers of moving water molecules (60 water molecules per bilayer) superimposed on 2 bilayers of fixed water molecules. The moving water molecules are treated as rigid rotors but were otherwise allowed to move according to Newton's equations of motion. To simulate an infinite surface, periodic boundary conditions were applied in the directions parallel to the scattering plane (x and y directions). The TIP4P potential[52] was used to describe the interaction between the water molecules, because it yields a stable hexagonal ice structure at the range of temperatures relevant to this study.[53,54] In this model, there are two positive charges on the hydrogen atoms (0.52 e) and a negative charge (-1.04 e) at a distance of 0.15 Å from the oxygen atom along the bisector of the HOH angle as shown in Figure 1a. The medium-range dispersion and short-range repulsion interaction between the water molecules are described using a Lennard-Jones LJ(12−6)[55] potential centered on the oxygen atoms. The initial configuration of the ice surface obeys the ice rules[56] and has a zero dipole moment. The surface was equilibrated at $T_s = 150$ K, using a computational analogue of a thermostat which was applied for typically 1 ps.[57] During this period, the velocities of the water molecules were rescaled with respect to the desired temperature as described in ref 57. The thermostat was then switched off, and the surface was left to equilibrate for approximately 100 ps before the scattering calculations were started. In the equilibration of the ice surface, a time step of 1 fs was used.

2.2. The CO−Ice Interaction. The CO−ice interaction has been constructed as a sum of CO−H_2O pair potentials, similar to the potentials for HCl−ice.[50] The CO−H_2O pair potential (PP) can be written as

$$V_{\mathrm{CO-H_2O}} = V_{\mathrm{els}} + V_{\mathrm{rep}} + V_{\mathrm{dis}} \tag{1}$$

where V_{els} represents the electrostatic interactions between the charges on the two molecules, V_{rep} represents the short-range repulsion energy, and V_{dis} represents the dispersion energy. The electrostatic interaction can be written as

$$V_{\mathrm{els}} = \sum_{i,j=1}^{4,3} \frac{q_i q_j}{r_{ij}} \tag{2}$$

where the charges q_i and q_j are charges on CO and H_2O, respectively, and r_{ij} is the distance between the two charges. The charges of CO were obtained from fitting a four-point charge model (shown in Figure 1b) to the electrostatic potential of an isolated CO molecule. The electrostatic potential of CO was obtained from ab initio calculations performed using the quantum chemistry package GAMESS US.[58] The calculations were performed at the MP2 level[59] of theory, using the 6-31G*,+ compatible basis set.[60] Both atoms are complemented with polarization functions (exp 0.80) and diffuse functions (exp 0.0438 for the C atom and exp 0.0845 for the O atom).

The dispersion energy was obtained from the dispersion part of the Lennard-Jones interaction potential between the i and j atoms of CO and water, respectively

$$V_{\mathrm{dis}} = -D(R_{ij}) \sum_{i,j=1}^{2,3} \frac{(c_6)_{ij}}{R_{ij}^{\;6}} \tag{3}$$

where the coefficient $(c_6)_{\mathrm{ij}} = 4\epsilon_{\mathrm{ij}}\sigma_{\mathrm{ij}}^{\;6}$ and R_{ij} is the distance between the atoms i and j of CO and the water molecule. The values of ϵ_{ij} and σ_{ij} were obtained from refs 51 and 61. The dispersion energy was damped by using the damping function:[62]

$$D(R) = \begin{bmatrix} 1.0, & R \geqslant 1.28R_{\mathrm{m}} \\ \exp\left(\dfrac{1.28R_{\mathrm{m}}}{R} - 1\right)^2, & R < 1.28R_{\mathrm{m}} \end{bmatrix} \tag{4}$$

The value of R_{m} for each pair of atoms of CO and H_2O was taken as the sum of the van der Waals radii of the two atoms. The values of the van der Waals radii given by Bondi[63] were used.

The short-range repulsion energy is written as

$$V_{\mathrm{rep}} = \sum_{i,j=1}^{2,3} \alpha_{ij} \exp(-\beta_{ij} R_{ij}) \tag{5}$$

The exponents β_{ij} and the preexponential coefficients α_{ij} were calculated by fitting the ab initio data for the CO−H_2O interaction to the pair potential (PP) expression given in eq 1. The CO−H_2O potential energies used for the fitting were based

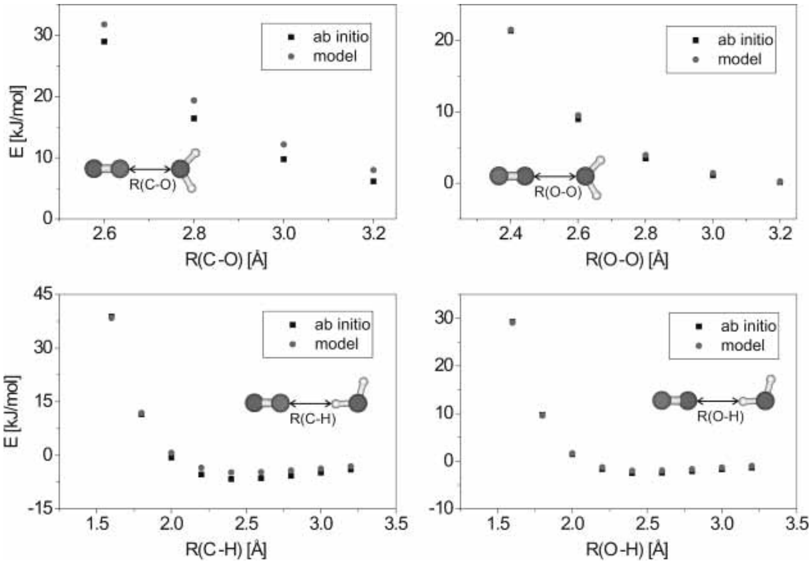

Figure 2. Interaction energies of CO−H$_2$O obtained from our potential fit (eq 1) plotted together with the energies of the complex obtained from ab initio calculations (see the text for more details). The energies are plotted as a function of the distance between the closest two atoms of the two different molecules for OC−OH$_2$ (a), CO−OH$_2$ (b), OC−HOH (c), and CO−HOH (d). In the illustrations, the gray large sphere represents the C atom, the dark sphere represents the O atom, and the small light gray spheres represent the H atoms.

TABLE 1: Values of the CO−H$_2$O Pair Potential Parameters[a]

pair	α_{ij} [kJ/mol]	β_{ij} [Å^{-1}]	$(c_6)_{ij}$ [kJ/molÅ^6]	R_m [Å]
C−H	23374.1	4.09	596.0	2.90
C−O	38979.0	2.77	1823.8	3.22
O−H	10406.0	3.61	434.9	2.72
O−O	149769.1	3.65	1350.8	3.04

[a] See the text for the meaning of the parameters.

on ab initio calculations for four different configurations (see the inset illustrations of the four configurations in Figure 2). The ab initio calculations of the CO−H$_2$O interactions were performed using the quantum chemistry package Gaussian 98.[64] The ab initio calculations were performed at the MP2 level of theory,[59] using a medium-polarized Sadlej basis set,[65] which consists of (10s6p4d/6s4p) contracted to [5s3p2d/3s2p]. This basis set has also been used before to obtain the CO−water intermolecular potential, and has been shown to be reliable in intermolecular forces calculations (see ref 66 and the references therein). The counterpoise correction of Boys and Bernardi for the interaction energies has also been applied,[67] because the size of the BSSE was found to be significant, which is expected for a weakly bonded system. The CO−H$_2$O potential was recalculated because the paper in which the CO−H$_2$O potential was calculated did not include tables or an analytical fit of the potential.[66] Also, the potential fit developed later and based on those ab initio calculations, as given in the appendix of ref 68, is too complicated to be used in molecular dynamics simulations. The values used for the parameters of the CO−H$_2$O potential given in eq 1 are listed in Table 1 and shown in Figure 1, parts a and b. Figure 2a−d shows the ab initio data together with the fitted energies obtained from our PP (eq 1). The figures show a fair agreement between the fitted and the ab initio energies, with a maximum underestimation of the binding energy of about 20% for the third configuration, i.e., OC−HOH.

The potential minimum configuration predicted by our PP is shown in Figure 3, in which CO forms an intermolecular bond with the water molecule though its carbon atom, with O−C−H and C−H−O$_w$ angles differing from 180°, where O$_w$ is the oxygen atom of the water molecule. This configuration is in reasonable agreement with the minimum geometry obtained from the ab initio calculations and with the geometry predicted by molecular electric resonance and Fourier transform microwave absorption spectroscopy experiments.[69] In the configuration shown in Figure 3, the distance between the center of mass of CO (COM) and O$_w$ is 4 Å and the C−H distance is 2.47 Å, with an O$_w$−H−C angle of 172°. The H−O$_w$−COM bond angle is 4.5°, with the O$_w$H bond pointing to the carbon atom of CO. The predicted distances and the nonlinear tilt of the interaction bond O$_w$−H−COM found using our potential are in good agreement with the experimental data and with the results of the ab initio calculations.[70]

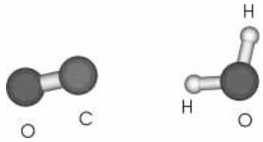

Figure 3. Optimized configuration of CO−H$_2$O complex, using our potential given in eq 1. See the text for discussion.

2.3. The CT Calculations. In the CT calculations, the H$_2$O−H$_2$O and the CO−H$_2$O interactions were set to zero at very long distances ($\geq$10 Å), by using a switching function.[50] The Monte Carlo technique[51] was used to select at random the initial orientation of CO and the impact position on the ice surface. The initial angular momentum of CO was set to be zero because our goal was to obtain predictions for molecular beam experiments in which the CO rotational temperature would be low. The calculations were performed for $T_s = 150$ K, for different incidence energies ($E_i = 9.6$, 24.1, 48.2, 96.5, and 193 kJ/mol) at normal incidence ($\theta_i = 0°$, θ_i being the angle between the surface normal and the incident velocity vector, i.e., the angle of incidence) and for $E_i = 48.2$ kJ/mol at off-normal incidence ($\theta_i = 20°$, 40°, and 60°).

For each set of conditions, 100 trajectories were computed. Each trajectory was run for 3 ps, using a time step of 1/9 fs. At the beginning of each trajectory, CO was placed 11.3 Å above the ice surface. To simulate the collision dynamics, Newton's equations of motion of the impinging molecule and the water molecules were integrated using an improved leapfrog algorithm.[71]

The ice surface was operationally defined to be at a height equal to $Z_s = 22.5$ Å (in the first monolayer, the upward pointing

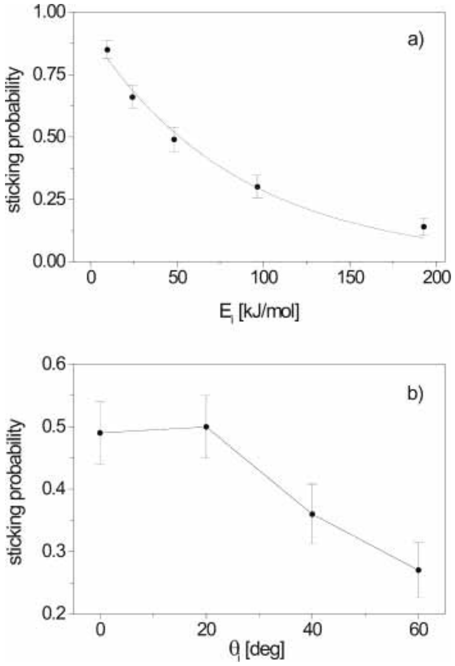

Figure 4. Sticking probability of CO to ice is plotted as a function of E_i for normal incidence (a), and as a function of θ_i at $E_i = 48.2$ kJ/mol (b). The solid line in a is an exponential decay fit of P_s.

hydrogen atoms are at about 22.7 Å, whereas the oxygen atoms are at about 21.7 Å). A sticking trajectory was defined as a trajectory which exhibits more than one turning point in the Z coordinate of CO for motion normal to the surface, with two additional requirements: (i) the final energy (E_f) of CO being trapped at the ice surface is below kT_s ($E_f < -1.25$ kJ/mol) and (ii) $Z_f \leq 26.5$ Å, where Z_f is the final Z coordinate of CO at the end of the trajectory. Here, the energy of the trapped molecule is the sum of its potential, translational, and rotational energy, where the zero of the potential energy is defined by CO in the gas phase. The second possibility is backscattering when CO returns to the gas phase ($Z_f \geq 29.5$ Å). At the end of the 3 ps run, if one of the two additional criteria used to define sticking is not yet met but $Z_f \leq 29.5$ Å so that the molecule cannot be classified yet as either stuck or scattered, the trajectory is run for an additional time (in some cases, for additional 6 ps) in order to distinguish between the two mechanisms. Surface penetration by CO was also considered as a possible second sticking mechanism. The operational definition of penetration used here is the same definition of HCl penetration used in ref 72; that is, penetration is defined to occur if the Z_f of CO falls below 22.5 Å.

3. Results and Discussion

3.1. Sticking. The computed sticking probability (P_s) of CO to ice is shown in Figure 4a as a function of E_i, for normal incidence at $T_s = 150$ K. The sticking probability decreases substantially with E_i and shows a monotonic decay with E_i.[73] P_s can be fitted to a decay function

$$P_s = A \exp(-BE_i)$$

where $A = 0.9$ and $B = 0.012$ (kJ/mol)$^{-1}$. The decrease of P_s with E_i arises because more energy has to be transferred to the surface at a higher E_i, for trapping to occur.

For off-normal incidence, assuming the ice surface to be structureless to the incident CO, one would expect P_s to increase with θ_i because the normal component of E_i required to be transferred to the surface for trapping to occur scales with $\cos^2(\theta_i)$. The CT calculations for off-normal incidence at $E_i = 48.2$ kJ/mol, however, show that P_s decreases with θ_i for $\theta_i > 20°$ as shown in Figure 4b. The reason for this decrease is that, at large values of θ_i, the impinging molecule interacts with a large number (> 2) of the surface water molecules, making the energy transfer from the impinging molecule to the ice surface less efficient at large θ_i (see below). In the approximation that CO and the ensemble of water molecules forming the collision center act as hard spheres, the amount of the energy transferred to the surface depends on the ratio of the total mass of the ensemble of the H_2O molecules making up the collision center and the mass of the incoming molecule as explained in detail in ref 46. The same trend was also found to occur in our study of sticking of HCl to ice at hyperthermal energies.[46]

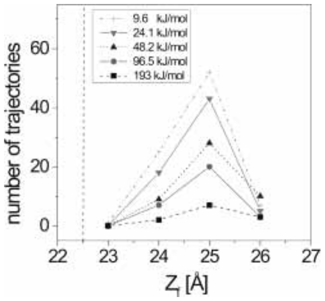

Figure 5. Number of sticking trajectories is plotted as a function of Z_f of CO, at $E_i = 9.6$, 24.1, 48.2, 96.4, and 193 kJ/mol for normal incidence. The dashed line represents the ice surface at 22.5 Å. Binning was used to assign the trajectories to integer values of Z_f.

For normal incidence, the number of sticking trajectories is plotted as a function of the final value of Z (Z_f) of CO at the end of those trajectories (Figure 5), for all values of E_i studied here. The figure shows that the sticking of CO to ice occurs via a single sticking mechanism, CO being adsorbed on top of the ice surface, i.e., adsorption. Most sticking (adsorbing) trajectories end with the adsorbed CO on top of the ice surface, at a distance of 2−3 Å from the surface, which is represented by the dotted line in Figure 5. This is in agreement with the results of ab initio calculations performed on CO adsorption to a perfect ice lattice of two bilayers.[31] In our calculations, even at the highest E_i (193 kJ/mol), we have not seen any case of CO penetrating the surface ($Z_f \leq 22.5$ Å), a second mechanism of sticking which we found to occur in the case of HCl sticking to ice at moderately low E_i (as low as 96.4 kJ/mol).[46] The penetration of HCl into the ice was found to be efficient mainly due to the open structure of the surface.

Because CO is a small molecule (the van der Waals radii of the C and the O atoms are about the same as that of the Cl atom), one would expect also that CO could penetrate the surface. Instead, at the highest E_i, we found that the impinging CO could damage the surface, which we did not observe in the case of HCl. Figure 6a is a snapshot of CO approaching the hexagonal ice surface just before the collision. The surface damage due to the CO collision is significant and involves several water hexagonal rings, as shown in a snapshot of the system shortly after the collision (Figure 6b). At the first turning point of the Z coordinate of CO for motion normal to the surface, i.e., when CO gets close to the surface, the surface is deformed such that CO, oriented perpendicular to the surface, becomes the center of a large cavity in the first surface bilayer. Most of the trajectories for which surface damage was observed correspond to trajectories in which CO hits the surface in the middle of a hexagonal water ring, as illustrated in Figure 6a. Interestingly, for such geometries, penetration was found to occur in

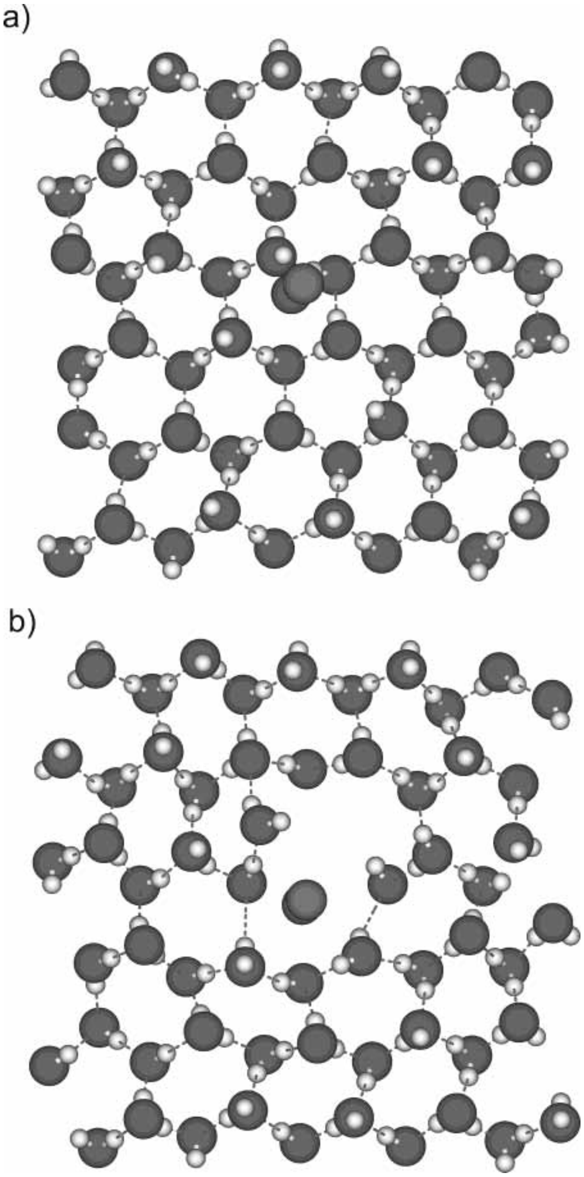

Figure 6. Snapshot of the normally incident molecule approaching the ice surface just before the collision occurs (a). A snapshot of the surface with disordered hexagons due to the CO collision with the surface (b).

the case of HCl scattering from ice.[46,72] The deformation has been observed for the case of sticking and also for the case of backscattering at $E_i = 193$ kJ/mol.

To understand why CO does not penetrate the surface, calculations of the potential energy of CO interacting with a static ice surface were performed. In these calculations, the potential energy of CO was minimized with respect to the CO orientation while moving along the central axis of a water hexagonal shaft (examining the interaction for several shafts, which run perpendicular to the ice surface). Figure 7 shows the CO−ice interaction as a function of the translational coordinate Z of CO for a representative example. On its way into the ice, CO moves through an attractive physisorption well with a depth of about 13.3 kJ/mol. For penetration to occur, CO has to overcome a barrier that is about 178 kJ/mol even when minimized with respect to the CO orientation (for comparison, in the case of HCl, the barrier height for penetration is about 50 kJ/mol). This represents the minimum barrier we have found in our calculations which involve several hexagonal shafts of the basal plane face (0001). The attractive well depth and the barrier height for penetration differ from one hexagonal shaft to the other. The barrier height varies between 178 and 280 kJ/mol. Figure 7 shows that the least unfavorable configuration of CO in the ice surface corresponds to CO in an interstitial position between the ice bilayers (with CO oriented nearly perpendicular to the surface, not shown), with a potential energy (E_{pot}) of +93 kJ/mol between the first and the second bilayer and +84 kJ/mol between the second and the third bilayer (0 kJ/mol corresponds to CO in the gas-phase). This is in reasonable agreement with the results of ab initio calculations, which found that the total energy of the interstitial CO−ice lattice system is 78 kJ/mol higher than the sum of the energies of the two subsystems.[31] In those calculations, the least unfavorable configuration was likewise found to correspond to an interstitial, nearly perpendicular CO, located along the central axis of the hexagonal shaft, at an equal distance from the surface two bilayers (in the ab initio calculations, the model ice lattice consisted of two surface bilayers[31]).

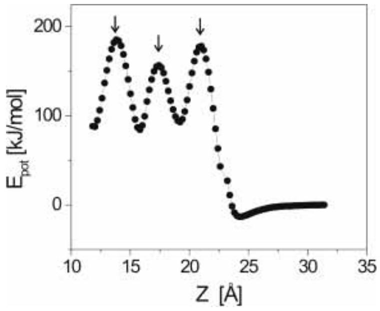

Figure 7. Potential of CO interacting with a static ice surface shown as a function of the translational *Z* coordinate of CO normal to the surface, CO moving along the central axis of a hexagonal water shaft. The periodic character of the curve reflects the periodicity of the ice surface in the direction normal to the surface. The positions of the maxima coincide with the positions of the surface bilayers.

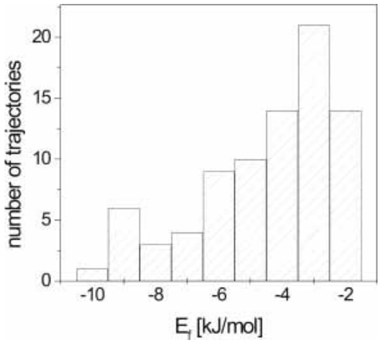

Figure 8. Histograms showing the number of sticking trajectories as a function of the final molecule-surface interaction energy (E_f, which is the sum of the potential, translational and rotational energy of CO) at $E_i = 9.6$ kJ/mol for normal incidence.

For normal incidence, Figure 8 shows histograms of the number of the adsorbing trajectories calculated at $E_i = 9.6$ kJ/mol, distributed over the final energy (E_f) of CO at the end of the trajectories, i.e., the binding energy. The average binding energy of CO, $\langle E_f \rangle$, is 4.33 kJ/mol. The maximum value of E_f is about 10.0 kJ/mol, which is in good agreement with the ab initio value for CO interacting with a model ice lattice.[31] This value is also in good agreement with the binding energy of CO to ice (10.0 kJ/mol) found in Fourier transform infrared spectroscopy (FT-IR) experiments.[31] The maximum value of the binding energy we find also agrees well with the binding energy (about 10.4 kJ/mol) found in volumetric and FT-IR isotherm experiments.[33,35]

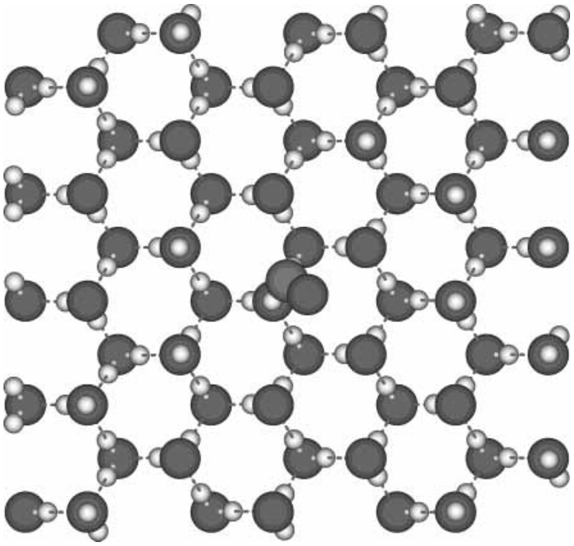

Figure 9. Optimized geometry of CO interacting with a static ice surface shown, using the same color code of the atoms as in Figure 2.

Geometry minimizations of CO adsorbed on top of a static ideal (0001) crystalline surface were carried out to obtain further insight into the possible CO−ice configurations, especially the adsorbing sites which yield the maximum binding energy. The potential energy minima for the CO molecule interacting with the static ice surface were found to lie in the range of −14.2 to −9.3 kJ/mol. In the first monolayer (ML1) of the ice surface, the water molecules can have six possible orientations. In three of these orientations (class 1), the water molecule has one of its protons pointing upward, away from the surface. In the other three orientations (class 2), the water molecule has both protons pointing obliquely down to the water molecules in the second monolayer (ML2). The calculations show that the most stable configuration corresponds to CO interacting with a dangling OH group of a class 1 molecule, as shown in Figure 9. This is consistent with the experimental results, which have shown that this site is the most stable adsorption site, and corresponds to the secondary band at 2152 cm^{-1}.[31,33−37,39]

Our finding of dangling OH as the most stable adsorption site is also in agreement with results of the geometry optimization of the system as obtained from ab initio calculations.[31,39] However, in our calculations, the molecule is not perpendicular to the surface, as found in the calculations of refs 31 and 39, but is nearly parallel to surface. This might be due to the nature of the surface used in the ab initio calculations: in that surface, the water molecules are arranged in a highly ordered way (in the first monolayer, the water molecules are arranged in rows such that in a particular row either all molecules point one proton up (class 1) or all of them point both protons down (class 2)). This type of configuration leads to a strong electric field on top of the model ice lattice.

According to our geometry optimization calculations, CO can also be adsorbed on top of a surface hexagonal ring, interacting with an oxygen atom of a water molecule of class (2) with a dangling electron pair (dO site) or interacting with an oxygen atom of a four-coordinated water molecule in ML2 (s4 site). In these configurations, CO is nearly parallel to the surface. The two surface adsorbing sites have been observed in the volumetric and FT-IR isotherm measurements of CO adsorption on amorphous ice.[35,74] Although these sites were not identified as adsorbing sites in the ab initio calculations of ref 31 (these configurations were found to be not stable), our findings are consistent with recent experiments on CO adsorption to ice covered by CF_4[35] and with recent DFT based calculations.[39]

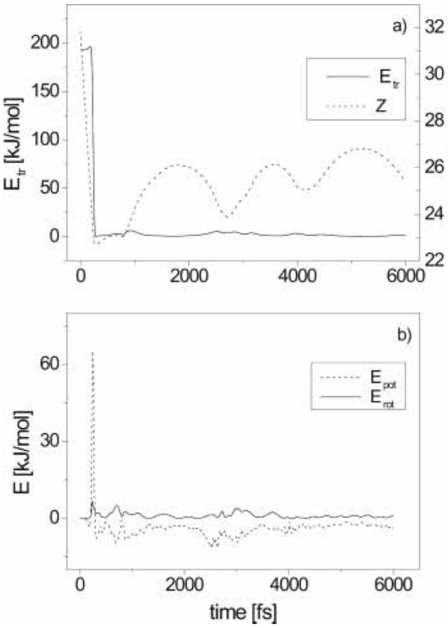

Figure 10. E_{tr} plotted together with the normal coordinate Z of CO (a) and the energies E_{rot} and E_{pot} (b) plotted as a function of time for a typical adsorbing trajectory at $E_i = 193$ kJ/mol, for normal incidence.

Figure 10a shows the translational energy (E_{tr}) of CO, plotted as a function of time together with the Z coordinate of CO for a typical adsorbing trajectory at $E_i = 193$ kJ/mol and $\theta_i = 0°$. The energy transfer to the surface is very efficient: most of E_{tr} is transferred to the surface within 0.5−1.0 ps, similar to what we found for the case of HCl scattering from ice.[46] The large variation observed in the Z coordinate of CO indicates the weakness of the CO binding to the ice surface. The potential energy (E_{pot}) reaches a maximum value (about 40% of E_i) when CO reaches the surface (Figure 10b). The rotational energy (E_{rot}) also increases when CO reaches the surface, but less than E_{pot}.

3.2. Scattering. For the case of backscattering, the molecule is scattered to the gas phase after a single collision with the surface for most of the trajectories, as illustrated in Figure 11a for a typical backscattering trajectory at $E_i = 193$ kJ/mol and $\theta_i = 0°$. The figure shows that the energy transfer to the surface occurs in a very short period of time, as was the case for sticking (see Figures 10a and 11a). The energies E_{pot} and E_{rot} increase when CO reaches the surface, see Figure 11b. The scattered molecule retains a significant part of the E_{rot}, which was initially gained by the molecule upon the collision with the surface.

For normal incidence, Figure 12, parts a and b, shows histograms of the final energy (E_f), defined as the sum of the translational and the rotational energy of the scattered CO, for $E_i = 96.5$ and 193 kJ/mol, respectively. The figures show that most of E_i of CO is transferred to the surface, E_f of CO being below 20 kJ/mol in most of the trajectories, for both incidence energies. At $E_i = 193$ kJ/mol, the scattered CO loses up to 90% of its translational energy, yet P_s is very low ($P_s = 0.15$ at $E_i = 193$ kJ/mol) compared to the efficient sticking in the case of HCl[46,72] at the same E_i and θ_i (for the case of HCl, $P_s = 0.95$ at $E_i = 193$ kJ/mol).

At this point, we can only compare our results for the average final kinetic energies of the scattered CO at normal incidence to the results of molecular beam experiments performed to study the inelastic scattering of N_2 from ice surfaces, which were also performed at normal incidence, for $E_i = 8.7$, 33.8, and 72.4 kJ/mol at $T_s = 100$ and 150 K.[43] N_2 is a molecule similar to CO and has the same mass. In the experiments, two scattering

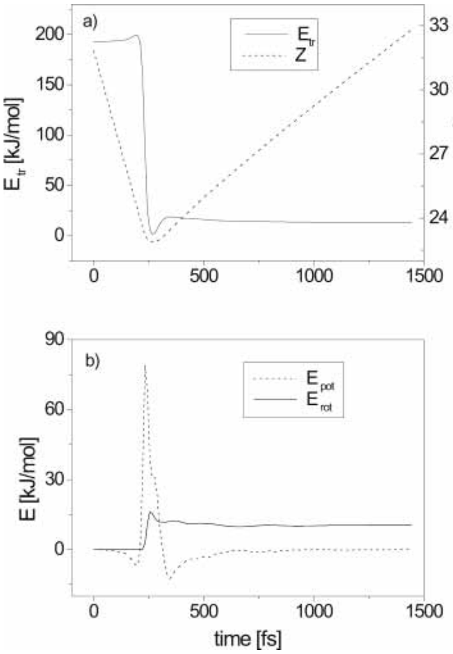

Figure 11. E_{tr} plotted together with the normal coordinate Z of CO (a) and the energies E_{rot} and E_{pot} (b) plotted as a function of time for a typical backscattering trajectory at $E_i = 193$ kJ/mol, for normal incidence.

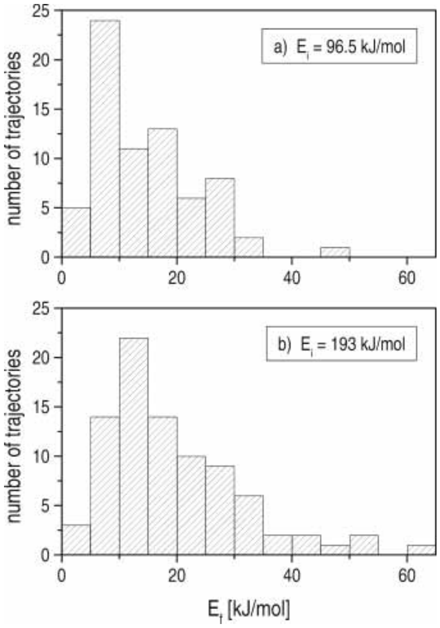

Figure 12. Histograms of the number of backscattering trajectories distributed over E_f of the scattered CO (the sum of the final translational and rotational energy of CO) shown for $E_i = 96.5$ kJ/mol (a) and 193 kJ/mol (b), at normal incidence.

channels were observed: a direct inelastic channel and a trapping desorption channel. Most of our trajectories are classified as direct scattering: most of the trajectories are scattered back after a single (or double) collision and therefore belong to the first scattering channel. Thus, we have compared our results with the results of the molecular beam experiments for the first channel only, at $T_s = 150$ K.[43] In Figure 13, parts a and b, the calculated average values of the final E_{tr} and E_{rot} are compared with the experimental values for the direct scattering channel of N_2.[75] The figures show that the average final values of E_{tr} and E_{rot} increase with E_i as expected. This increase is in agreement with the experimental results of N_2.

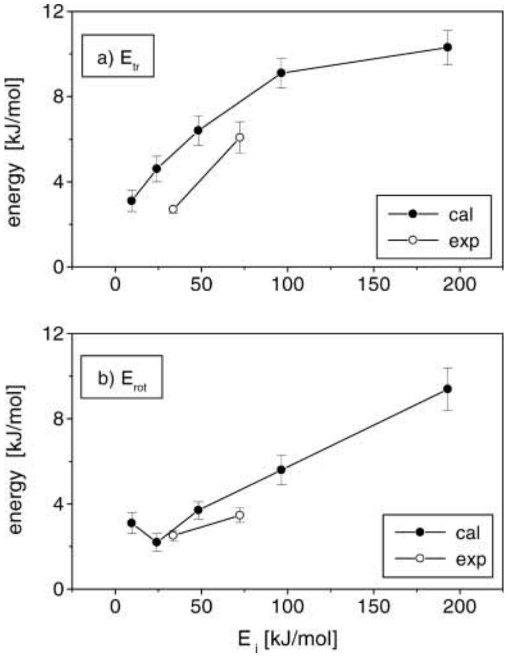

Figure 13. Calculated average values of the final E_{tr} (a) and E_{rot} (b) of backscattered CO (solid symbols) plotted together with the experimental results (open symbols)[43] for the direct scattering channel of N_2 as a function of E_i, for normal incidence at $T_s = 150$ K.

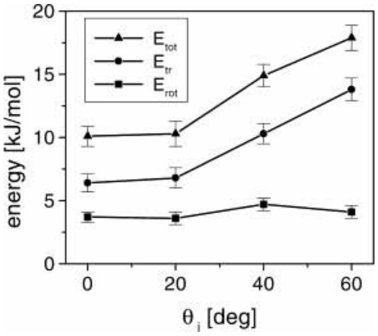

Figure 14. Average values of the final E_{tr}, E_{rot}, and E_f plotted as a function of θ_i for the case of backscattering at $E_i = 48.2$ kJ/mol for off-normal incidence.

The theoretical and experimental data show that the energy transfer to the ice surface is quite efficient. Quantitatively, a difference with the experimental results is that the calculated average values of the final translational energy of the scattered CO molecules are somewhat larger than the values measured for N_2. However, the curves representing the final values of $\langle E_{rot}\rangle$ are in reasonable agreement with one another.

For off-normal incidence, substantial backscattering occurs: at $\theta_i = 60°$ and $E_i = 48.2$ kJ/mol, more than 70% of the trajectories are classified as backscattering trajectories. The energy transfer to the surface becomes less efficient at $\theta_i > 20°$, as shown in Figure 14, and this causes the decrease of P_s with θ_i, for $\theta_i > 20°$ (see Figure 4b). At large θ_i, the scattered molecule retains a large part of its kinetic energy, mainly as translational energy. The final rotational energy hardly depends on θ_i. Figure 15a−d shows histograms of the number of backscattering trajectories for $E_i = 48.2$ kJ/mol, distributed over the final total energy of the scattered molecule for $\theta_i = 0°$, 20°, 40°, and 60°, respectively. The figure shows that, at $\theta_i = 60°$ and $E_i = 48.2$ kJ/mol, CO retains more than 60% of its E_i in some of the trajectories, similar to what we have obtained in our study on HCl.[46] This is also in qualitative agreement with the results of molecular beam experiments on HCl scattering

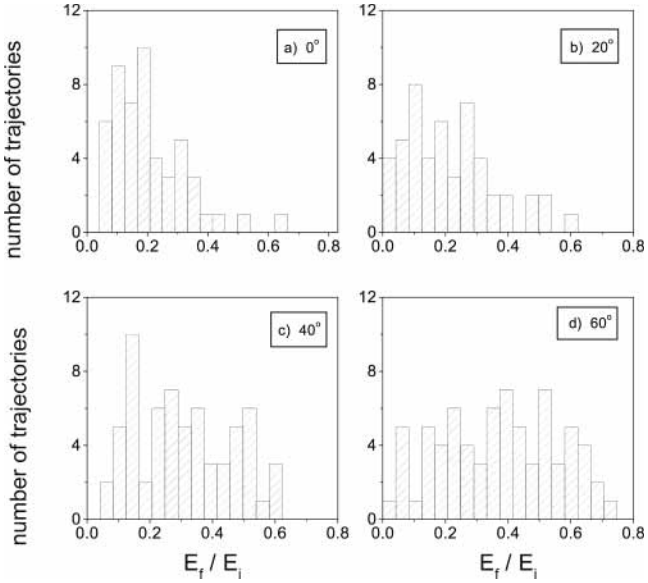

Figure 15. Histograms showing the number of backscattering trajectories distributed over the final energy of the scattered CO (E_f) for off-normal incidence, for $\theta_i = 0°$ (a), 20° (b), 40° (c), and 60° (d) at $E_i = 48.2$ kJ/mol.

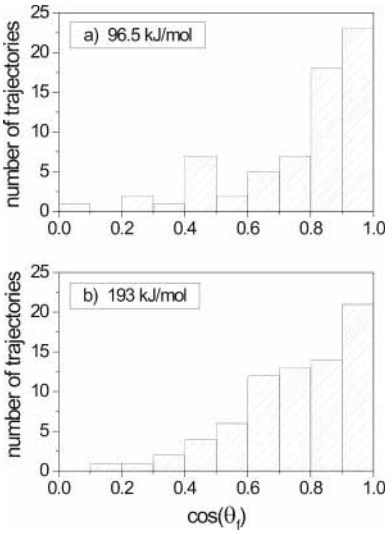

Figure 16. Histograms showing the number of backscattering trajectories as a function of $\cos(\theta_f)$ at $E_i = 96.5$ (a) and 193 kJ/mol (b), for scattering at normal incidence.

from ice surfaces,[44] which found that, at $E_i = 51$ kJ/mol and $\theta_i = 70°$, HCl retains up to 45% of its initial translational energy, depending on the final scattering angle.

The number of backscattering trajectories has been plotted in histograms distributed over cos θ_f at $E_i = 96.4$ and 193 kJ/mol in Figure 16, parts a and b, respectively, for normal incidence, where θ_f is the final angle of the scattered CO molecule from the surface normal. The figures show that most of the CO molecules are scattered at small θ_f (close to the surface normal). Figure 17 shows a polar plot of E_f of CO as a function of θ_f for backscattering trajectories at $E_i = 48.2$ kJ/mol for off-normal incidence at $\theta_i = 60°$. The figure shows that the molecules scattered at large θ_f are on the average translationally hotter than those scattered at small θ_f, similar to what we have found in our study on HCl scattering from ice (0001) surface[46] at a larger incidence energy ($E_i = 193$ kJ/mol), for the same value of θ_i. This trend was also observed in molecular beam experiments performed on HCl scattering from crystalline ice, for $\theta_i = 70°$ and $E_i = 51$ kJ/mol.[44]

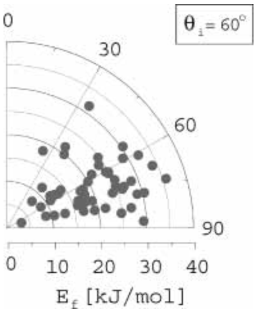

Figure 17. Polar plot of θ_f as a function of E_f shown for $E_i = 48.2$ kJ/mol, for off-normal incidence at $\theta_i = 60°$.

4. Conclusions

In this paper, we have presented the results of classical trajectory calculations on the sticking of hyperthermal CO to the basal plane face of crystalline ice. The calculations show that P_s decreases significantly with E_i, and with θ_i for $\theta_i > 20°$. The predicted quantitative dependence of P_s on E_i and θ_i can be confirmed experimentally, by using molecular beam experiments on scattering of CO from ice for normal and off-normal incidence. We have not seen any case of surface penetration for the CO + ice(0001) system, in contrast to our predictions for HCl + ice(0001).[72] Instead, we find that CO can deform the ice surface, such that CO becomes the center of a large cavity in the first surface bilayer, especially when CO hits the surface in the center of a hexagonal water ring. Calculations of the potential energy of CO interacting with a static ice lattice along the axis of a hexagonal shaft show a barrier of more than 178 kJ/mol to penetration (compared to a value of 50 kJ/mol in the case of HCl[46]).

In the case of sticking, CO is trapped on top of the ice surface, at a distance of 2−3 Å, in agreement with the results of ab initio calculations.[31] The molecule is trapped over a dangling OH group, which corresponds to the minor CO infrared band at 2152 cm^{-1}. It can also be adsorbed on top of a surface hexagonal ring, interacting with a dangling electron pair oxygen atom of a water molecule in the first or the second monolayer (the dO and 4s adsorbing sites respectively), which corresponds to the major CO infrared band at 2139 cm^{-1} at low CO coverage. Our findings are in agreement with the measured infrared bands corresponding to these adsorbing sites.[31,33−37]

The average binding energy of the trapped molecule is 4.33 kJ/mol, with a maximum value of 10.4 kJ/mol. The latter value is in good agreement with the measured binding energies[31,33,35] and also with the results of ab initio calculations.[31]

For normal incidence, the energy transfer from the impinging molecule to the surface is efficient and fast. Most of E_i is transferred to the surface in a single collision (within 1 ps). However, the efficiency of the energy transfer decreases with θ_i: in some trajectories, the scattered CO retains more than 60% of its E_i, mostly as translational energy, at $\theta_i = 60°$ and $E_i = 48.2$ kJ/mol.

The calculations show that most of the backscattering occurs in trajectories exhibiting a single or a double collision with the surface. The average final values of E_{tr} and E_{rot} increase with E_i, in agreement with the results of N_2 scattering from ice experiments.[43] The final $\langle E_f \rangle$ increases with θ_i, mainly due to the increase in the final $\langle E_{tr} \rangle$.

For the case of backscattering at normal incidence, CO is scattered at small θ_f, close to the surface normal. For off-normal incidence ($\theta_i = 60°$), the hotter molecules scatter at larger θ_f, as was found in our previous calculations on HCl scattering from ice[46] and in molecular beam experiments on HCl + ice.[44]

Acknowledgment. This research is part of the program of FOM and is financially supported by NWO. We acknowledge allocations of computer time by the national Computing Facilities Foundation (NSF).

References and Notes

(1) Solomon, S. *Nature* **1990**, *347*, 347.

(2) Molina, M. J. *Angew. Chem., Int. Ed. Engl., Nobel Lecture* **1996**, *35*, 1778.

(3) Solomon, S. *Rev. Geophys.* **1999**, *37*, 275.

(4) Rowland, F. S. *Angew. Chem., Int. Ed. Engl., Nobel Lecture* **1996**, *35*, 1786.

(5) Ehrenfreund, P.; Schutte, W. A. In *Astrochemistry: From Molecular Clouds to Planetary Systems*; Mink, Y. C., van Dischoeck, E. F., Eds.; IAU Symposium, ASP: San Francisco, CA, 2000; Vol. 197, page 135.

(6) Tielens, A. G. G. M.; Tokunaga, A. T.; Geballe, T. R.; Baas, F. *Astrophys. J.* **1991**, *381*, 181.

(7) Tanaka, M.; Nagata, T.; Sato, S.; Yamamoto, T. *Astrophys. J.* **1994**, *430*, 779.

(8) Chiar, J. E.; Adamson, A. J.; Kerr, T. H.; Whittet, D. C. B. *Astrophys. J.* **1995**, *455*, 234.

(9) Allamandola, L. J.; Bernstein, M. P.; Sandford, S. A.; Walker, R. L. *Space Sci. Rev.* **1999**, *90*, 219.

(10) Hagen, W.; Tielens, A. G. G. M.; Greenberg, J. M. *Chem. Phys.* **1981**, *56*, 267.

(11) Maldoni, M. M.; Robinson, G.; Smith, R. G.; Duley, W. W.; Scott, A. *Mon. Not. Astron. Soc.* **1999**, *309*, 325.

(12) Chakarov, D.; Kasemo, B. *Phys. Rev. Lett.* **1998**, *81*, 5181.

(13) Malfait, K.; Waelkens, C.; Waters, L. B. F. M.; Vandenbussche, B.; Huygen, E.; de Graauw, M. S. *Astron. Astrophys.* **1998**, *332*, L25.

(14) d'Hendecourt, L. B.; Jourdain de Muzion, M. *Astron. Astrophys.* **1989**, *223*, L5.

(15) Whittet, D. C. B.; Gerakines, P. A.; Tielens, A. G. G. M.; Adamson, A. J.; Boogert, A. C. A.; Chiar, J. E.; de Graauw, T.; Ehrenfreund, P.; Prusti, T.; Schutte, W. A.; Vandenbussche, B.; van Dishoeck, E. F. *Astrophys. J.* **1998**, *498*, L159.

(16) Gerakines, P. A.; Whittet, D. C. B.; Ehrenfreund, P.; Boogert, A. C. A.; Tielens, A. G. G. M.; Schutte, W. A.; Chiar, J. E.; van Dishoeck, E. F.; Prusti, T.; Helmich, F. P.; de Graauw, T. *Astrophys. J.* **1999**, *522*, 357.

(17) Boogert, A. C. A.; Ehrenfreund, P.; Gerakines, P. A.; Tielens, A. G. G. M.; Whittet, D. C. B.; Schutte, W. A.; van Dishoeck, E. F.; de Graauw, T.; Decin, L.; Prusti, T. *Astron. Astrophys.* **2000**, *353*, 349.

(18) van Dishoeck, E. F.; Helmich, F. P.; de Graauw, T.; Black, J. H.; Boogert, A. C. A.; Ehrenfreund, P.; Gerakines, P. A.; Lacy, J. H.; Millar, T. J.; Schutte, W. A.; Tielens, A. G. G. M.; Whittet, D. C. B.; Boxhoorn, D. R.; Kester, D. J. M.; Leech, K.; Roelfsema, P. R.; Salama, A.; Vandenbussche, B. *Astron. Atsrophys.* **1996**, *315*, L349.

(19) Allamandola, L. J.; Sandford, S. A.; Valero, G. J. *Icarus* **1988**, *76*, 225.

(20) Grim, R. J. A.; Greenberg, J. M.; de Groot, M. S.; Baas, F.; Schutte, W. A.; Schmitt, S. B. *Astron. Astrophys.* **1989**, *78*, 161.

(21) Watanabe, N.; Kouchi, A. *Astrophys. J.* **2002**, *567*, 651.

(22) d'Hendecourt, L. B.; Allamandola, L. J.; Grim, R. J. A.; Greenberg, J. M. *Astron. Astrophys.* **1986**, *158*, 119.

(23) Sandford, S. A.; Allamandola, L. J.; Tielens, A. G. G. M.; Valero, G. J. *Astrophys. J.* **1988**, *329*, 498.

(24) Gerakines, P. A.; Scutte, W. A.; Ehrenfreund, P. *Astron. Astrophys.* **1996**, *312*, 289.

(25) Schriever, R.; Chergui, M.; Kunz, H.; Stepanenko, V.; Schwentner, N. *J. Chem. Phys.* **1989**, *91*, 4128.

(26) van Harrevelt, R. Photodissociation of water. Ph.D. Thesis, Leiden University, Leiden, The Netherlands, 2001.

(27) de Graauw, T.; Whittet, D. C. B.; Gerakines, P. A.; Bauer, O. H.; Beintema, D. A.; Boogert, A. C. A.; Boxhoorn, D. R.; Chiar, J. E.; Ehrenfreund, P.; Feuchtgruber, H.; Helmich, F. P.; Heras, A. M.; Huygen, R.; Kester, D. J. M.; Kunze, D.; Lahuis, F.; Leech, K. J.; Lunz, D.; Morris, P. W.; Prusti, T.; Roelfsema, P.; Salama, A.; Schaeidt, S. G.; Schutte, W. A.; Spoon, H. W. W.; Tielens, A. G. G. M.; Valentijn, E. A.; Vandenbusshe, B.; van Dishoeck, E. F.; Wesselius, P. R.; Wieprecht, E.; Wright, C. M. *Astron. Astrophys.* **1996**, *315*, L345.

(28) Roser, J. E.; Vidali, G.; Manicó, G.; Pirronello, V. *Astrophys. J.* **2001**, *555*, L61.

(29) Jaffe, J. E.; Hess, A. C. *J. Chem. Phys.* **1996**, *104*, 3348.

(30) Casanovas, J.; Pacchioni, G. *Chem. Phys. Lett.* **1996**, *259*, 438.

(31) Allouche, A.; Verlaque, P.; Pouricin, J. *J. Phys. Chem. B* **1998**, *102*, 89.

(32) Girardet, C.; Toubin, C. *Surf. Sci. Rep.* **2001**, *44*, 163.

(33) Manca, C.; Roubin, P.; Martin, C. *Chem. Phys. Lett.* **2000**, *330*, 21.

(34) Martin, C.; Manca, C.; Roubin, R. *Surf. Sci.* **2002**, *502*−*503*, 275.

(35) Martin, C.; Manca, C.; Roubin, R. *Surf. Sci.* **2002**, *502*−*503*, 280.

(36) Devlin, J. P. *J. Phys. Chem.* **1992**, *96*, 6185.

(37) Palumbo, M. E. *J. Phys. Chem. A* **1997**, *101*, 4298.

(38) van Duijneveldt, F. B.; van Duijneveldt-van De Rijdt, J. G. C. M.; van Lenthe, J. H. *Chem. Rev.* **1994**, *94*, 1873.

(39) Manca, C.; Martin, C.; Allouche, A.; Roubin, P. *J. Phys. Chem. B* **2001**, *105*, 12861.

(40) Devlin, J. P.; Buch, V. *J. Phys. Chem.* **1995**, *99*, 16534.

(41) Collings, M. P.; Dever, J. W.; Fraser, H. J.; McCoustra, M. R. S.; Williams, D. A. *Astrophys. J.* **2003**, *583*, 1058.

(42) Buch, V.; Delzeit, L.; Blackledge, C.; Devlin, J. P. *J. Phys. Chem.* **1996**, *100*, 3732.

(43) Gotthold, M. P.; Sitz, G. O. *J. Phys. Chem. B* **1998**, *102*, 9557.

(44) Andersson, P. U.; Någård, M. B.; Pettersson, J. B. C. *J. Phys. Chem. B* **2000**, *104*, 1596.

(45) Andersson, P. U.; Någård, M. B.; Svanberg, M.; Pettersson, J. B. C. *J. Phys. Chem. A* **2000**, *104*, 2681.

(46) Al-Halabi, A.; Kleyn, A. W.; Kroes, G. J. *J. Chem. Phys.* **2001**, *115*, 482.

(47) Al-Halabi, A.; van Dishoeck, E. F.; Kroes, G. J. *J. Phys. Chem. B* Submitted.

(48) Al-Halabi, A.; Fraser, H. J.; van Dishoeck, E. F.; Kroes, G. J. *Astrophys. J.* Submitted.

(49) Porter, R. N.; Raff, L. M. *Dynamics of Molecular Collisions, Part B*; Plenum: New York, 1976.

(50) Kroes, G. J.; Clary, D. C. *J. Phys. Chem.* **1992**, *96*, 7079.

(51) Allen, M. P.; Tildesley, D. J. *Computer Simulations of Liquids*; Clarendon: Oxford, U.K., 1987.

(52) Jorgensen, W. L.; Chandrasekhar, J.; Madura, J. D.; Impey, R. W.; Klein, M. L. *J. Chem. Phys.* **1983**, *79*, 926.

(53) Kroes, G. J. *Surf. Sci.* **1992**, *275*, 365.

(54) Karim, O. A.; Haymet, A. D. J. *J. Chem. Phys.* **1988**, *89*, 6889.

(55) Lennard-Jones.; Devonshire, A. F. *Nature* **1936**, *137*, 1069.

(56) Bernal, J. D.; Fowler, R. H. *J. Chem. Phys.* **1933**, *1*, 515.

(57) Berendsen, H. J.; Postma, J. P. M.; van Gunsteren, W. F.; DiNola, A.; Haak, J. R. *J. Chem. Phys.* **1984**, *81*, 3684.

(58) Schmidt, M. W.; Baldridge, K. K.; Boatz, J. A.; Elbert, S. T.; Gordon, M. S.; Jensen, J. H.; Koseki, S.; Matsunaga, N.; Nguyen, K. A.; Su, S. J.; Windus, L. T.; Dupuis, M.; Montgomery, J. A. *J. Comput. Chem.* **1993**, *14*, 1347.

(59) Möller, C.; Plesset, M. S. *Phys. Rev.* **1934**, *46*, 618.

(60) Francl, M. M.; Pietro, W. J.; Hehre, W. J.; Binkley, J. S.; Gordon, M. S.; DeFrees, D. J.; Pople, J. A. *J. Chem. Phys.* **1982**, *77*, 3654.

(61) Wales, D. J.; Popelier, P. L. A.; Stone, A. J. *J. Chem. Phys.* **1995**, *102*, 5551.

(62) Ahlrichs, R.; Penco, R.; Scoles, G. *Chem. Phys.* **1977**, *19*, 119.

(63) Bondi, A. *J. Phys. Chem.* **1964**, *68*, 441.

(64) Frisch, M. J.; Trucks, G. W.; Schlegel, H. B.; Scuseria, G. E.; Robb, M. A.; Cheeseman, J. R.; Zakrzewski, V. G.; Montgomery, J. A., Jr.; Stratmann, R. E.; Burant, J. C.; Dapprich, S.; Millam, J. M.; Daniels, A. D.; Kudin, K. N.; Strain, M. C.; Farkas, O.; Tomasi, J.; Barone, V.; Cossi, M.; Cammi, R.; Mennucci, B.; Pomelli, C.; Adamo, C.; Clifford, S.; Ochterski, J.; Petersson, G. A.; Ayala, P. Y.; Cui, Q.; Morokuma, K.; Malick, D. K.; Rabuck, A. D.; Raghavachari, K.; Foresman, J. B.; Cioslowski, J.; Ortiz, J. V.; Stefanov, B. B.; Liu, G.; Liashenko, A.; Piskorz, P.; Komaromi, I.; Gomperts, R.; Martin, R. L.; Fox, D. J.; Keith, T.; Al-Laham, M. A.; Peng, C. Y.; Nanayakkara, A.; Gonzalez, C.; Challacombe, M.; Gill, P. M. W.; Johnson, B. G.; Chen, W.; Wong, M. W.; Andres, J. L.; Head-Gordon, M.; Replogle, E. S.; Pople, J. A. *Gaussian 98*, revision A.5; Gaussian, Inc.: Pittsburgh, PA, 1998.

(65) Sadlej, A. J. *Collect Czech. Chem. Commun.* **1988**, *53*, 1995.

(66) Sadlej, J.; Buch, V. *J. Chem. Phys.* **1994**, *100*, 4272.

(67) Boys, S. F.; Bernardi, F. *Mol. Phys.* **1970**, *19*, 553.

(68) Sandler, P.; Buch, V.; Sadlej, J. *J. Chem. Phys.* **1996**, *105*, 10387.

(69) Yaron, D.; Peterson, K. I.; Zolandz, D.; Klemperer, W.; Lovas, F. J.; Suenram, R. D. *J. Chem. Phys.* **1990**, *92*, 7095.

(70) The experimental data[69] showed a nonlinear intermolecular CO−H_2O bond, with $\theta(\mathrm{H-O_w-COM}) = 11.5°$. The O_w−COM bond length is 4 Å, and the length of the C−H bond is 2.41 Å. The ab initio calculations[66] predicted the nonlinear hydrogen bond tilted by $\theta = 11°$, but with a very flat potential energy surface for $\theta = 0° - 20°$. The predicted O_w−COM bond length is also 4.0 Å. More recent ab initio calculations[31] on the CO−H_2O system showed that the OC−HOH configuration, the C−H distance is 2.422 Å, in good agreement with our results.

(71) Fincham, D. *Mol. Simul.* **1992**, *8*, 165.

(72) Al-Halabi, A.; Kleyn, A. W.; Kroes, G. J. *Chem. Phys. Lett.* **1999**, *307*, 505.

(73) Goodstein, D. M.; Dahl, E. B.; DiRubio, C. A.; Cooper, B. H. *Phys. Rev. Lett.* **1997**, *78*, 3213.

(74) Manca, C.; Allouche, A. *J. Chem. Phys.* **2001**, *114*, 4226.

(75) A model was built that had the complete velocity and angular distribution in it. The measured time-of-flight (TOF) data was fitted to this model, and then the total translational energy computed from the model distributions was reported. G. O. Sitz, private communication.